(Received 2 March 2024, Accepted 31 May 2024, Scheduled 12 June 2024)

Low-Profile Circularly Polarized Dual-Beam Holographic Antenna

Lanzheng Liu[1], Jincheng Xue[1], Ao Ni[2], Zhuopeng Wang[1], and Mingxiang Pang[1,*]

[1] College of Electronic and Information Engineering, Shandong University of Science and Technology, Qingdao, China
[2] College of Ocean Science and Engineering, Shandong University of Science and Technology, Qingdao, China

ABSTRACT: This paper presents the design of a low-profile circularly polarized dual-beam holographic antenna. Firstly, by employing a novel outer square inner circular (OSIC) structure as the basic unit of the hologram pattern, better performance is achieved for low-profile dielectric substrate holographic antennas. Secondly, a method of four-zone phase co-modulation is used to derive the impedance modulation formula of the hologram pattern. This formula was employed to model and generate a circularly polarized dual-beam holographic antenna, and the feasibility of theoretical analysis is verified through simulation and measurement. The antenna operates within the frequency range of 10.23 GHz to 16.59 GHz, with maximum gains of 16 dBi and 15.8 dBi for dual beams, respectively. The results indicate that this design method can realize circularly polarized dual-beam holographic antennas and provide some reference for satellite communication applications.

1. INTRODUCTION

With the advancement of wireless communication, holographic [1] antennas have become a hot topic in both theoretical and engineering research. Holographic antennas draw inspiration from the principles of optical holography, modulating leaky wave radiation at discontinuities in the surface structure as the surface wave propagates from the reference antenna, thereby further enhancing the gain of traditional antennas. Holographic antennas offer advantages such as low profile, lightweight, simple feed structure, and flexible construction [2]. Traditional holographic antennas place metal strips at the minima of holographic interference to generate secondary currents, achieving the design of specialized antennas and controlling the scattering of incident waves. At the beginning of the 21st century, square units [3] began replacing metal strips to form holographic patterns, where larger square units correspond to larger surface impedance values, enabling more precise control of electromagnetic waves. When using holographic patterns, which record the interference superposition of phase and amplitude between the reference antenna and the radiating antenna [4], with different impedance quasi-periodic elements, the surface waves of the antenna are modulated and utilized, forming predetermined leaky wave radiation [5]. Presently, research on holographic antennas is divided into multiple directions, such as specified beam radiation, multi-beam [6, 7], beam scanning [8], circular polarization (CP) [9, 10], miniaturization [11], low RCS [12], and conformal antennas [13].

As well known, in the modulation of leaky waves in holographic antennas, it is necessary to promote the excitation of surface waves. Therefore, the thickness of the dielectric substrate should exceed one-tenth of the effective wavelength [14]. Many holographic antennas use substrate thicknesses of 1.27 mm [15, 16], 1.5 mm [17, 18] and even thicker. These dielectric substrates exhibit relatively high thicknesses, which can be inconvenient for conformal applications. The substrate utilized in this paper is 0.635 mm thick. By employing the novel OSIC structure unit, more high-order harmonics can be excited, increasing the energy of high-order leaky modes, thereby enhancing the gain.

Today, multi-beam antennas are widely used in communication systems, allowing for the simultaneous transmission and reception of signals in different directions. They can also track multiple targets simultaneously in radar tracking systems [19]. Beam modulation in holographic antennas can be achieved using either co-modulation or zone modulation techniques. The former involves encoding the phase and amplitude information of multi-beam into the entire holographic pattern, with each unit participating in the modulation of all beams. The latter divides the hologram into multiple zones, with each zone implementing modulation for one beam, collectively achieving multi-beam capabilities. Additionally, circularly polarized antennas [20] can receive incident waves of arbitrary polarization, and their radiated waves can also be received by antennas of any polarization. Currently, circularly polarized holographic antennas typically utilize phase modulation techniques for implementation. Introducing a 90° phase shift in the orthogonal direction enables CP characteristics. This 90° phase shift introduces an orthogonal phase in circularly polarized wave radiation, thereby exciting a field distribution with equal magnitude but a 90° phase difference in the vertical direction, achieving the antenna's circularly polarized beam. Specifically, linearly polarized incident surface waves propagate through radiation to different phase quadrant units, resulting in the antenna emit-

* Corresponding author: Mingxiang Pang (pangmingxiang@sdust.edu.cn).

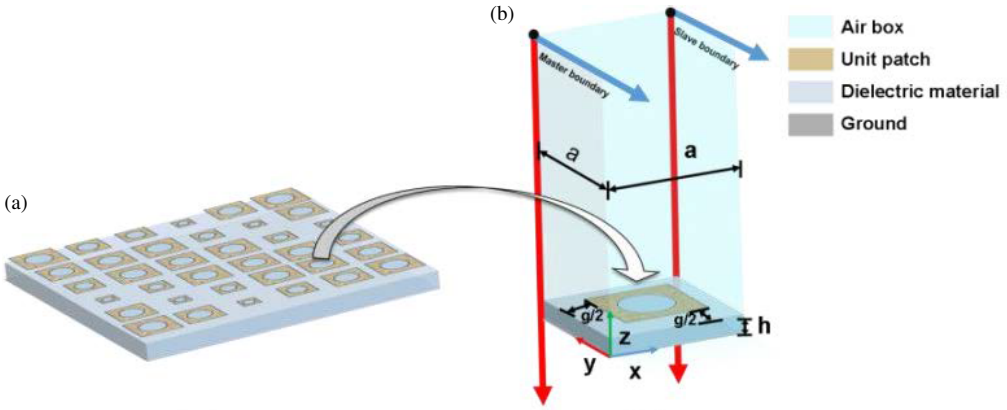

FIGURE 1. (a) Schematic diagram of the partial structure of the holographic antenna. (b) Schematic diagram of the unit simulation model of the holographic antenna.

ting circularly polarized leaky waves overall. Given these advantages and the lack of research on circularly polarized multi-beam holographic antennas, this design proposes a low-profile holographic antenna with circular polarization (CP) and dual beams, operating at a center frequency of 12 GHz. The antenna is fed using a single radiator, and its effectiveness and usability are verified through physical testing. The structure of the paper is organized as follows. Section 2 provides the design formulas, methods, and modeling of holographic antennas. In Section 3, we verify the feasibility of the proposed design through simulation and experimental measurements. Finally, Section 4 concludes the paper.

2. DESIGN FORMULA, METHOD AND MODELING OF HOLOGRAPHIC ANTENNAS

As depicted in Figure 1(a), the overall structure of the holographic antenna is composed of multiple units illustrated in Figure 1(b), where the radius of the circular elements synchronously varies with the length of the square units. Two pairs of master-slave boundaries are arranged in two directions within the air box, with phase differences of 0 and ϕ, respectively. The phase difference represents the phase delay incurred by the propagation of electromagnetic waves in that direction. The holographic antenna utilizes Rogers 3010 as its substrate material, with a thickness of 0.635 mm, a dielectric constant of 10.2, and a loss tangent of 0.0022. The top layer consists of units arranged in an OSIC structure, while the bottom layer acts as the ground plane.

As shown in Figure 2, electromagnetic simulation software HFSS was used to compare the intensity and vector direction of magnetic and electric fields for the OSIC unit and the square unit. In (a) and (b), the left portion displays the magnitude of the magnetic field for both units, represented by color, showing that the maximum magnetic field intensities for the two units are 150.5 T and 35.36 T, respectively. The lower right portion illustrates the surface magnetic field intensity for each unit, while the upper right portion depicts the vector direction of the magnetic field, where the length of the arrows is proportional to the magnetic field intensity. Compared to the 3 mm length of the unit, the proportionality coefficient is 85 T/mm. In (c) and (d), the left portion displays the magnitude of the surface current for both units, represented by color, indicating that the maximum surface current intensities for the two units are 296.38 T and 100.74 T, respectively. The right portion shows the vector direction of the current, with a proportionality coefficient of 185 T/mm. The comparison between the two units reveals that the OSIC unit has significantly higher magnetic field intensity and surface current intensity than the square unit, which will be reflected in the subsequent discussion of the data.

The refractive index of surface waves can be equivalently defined as the ratio of the speed of light in free space to the phase velocity of the surface wave:

$$n = \frac{c}{v_p} = \frac{\omega/v_p}{\omega/c} = \frac{k_t}{k_0} = \frac{\phi/a}{\omega/c} = \frac{\phi c}{a\omega} \tag{1}$$

According to Equation (1), the impedance (Z) of TM mode surface waves can be expressed as:

$$\begin{aligned} Z &= jZ_0 \frac{k_z}{k_0} = jZ_0 \frac{\sqrt{k_t^2 - k_0^2}}{k_0} = jZ_0 \sqrt{\left(\frac{k_t}{k_0}\right)^2 - 1} \\ &= jZ_0\sqrt{n^2-1} = jZ_0 \sqrt{\left(\frac{\phi c}{a\omega}\right)^2 - 1} \end{aligned} \tag{2}$$

where a represents the unit period, c the speed of light, ω the central frequency, v_p the phase velocity of the surface wave, k_z the wave number in the surface normal direction, k_t the wave number of the surface wave, k_0 the wave number in free space, and Z_0 the impedance of free space.

Different from the method of extracting intrinsic impedance by extracting eigenfrequencies [21], the approach of extracting intrinsic impedance through the difference between master and slave boundaries eliminates the need for cumbersome selection of suitable boundary differences. This helps prevent errors resulting from selecting inappropriate boundary differences and facilitates a more convenient and expedient acquisition of intrinsic impedance. By substituting the data of master-

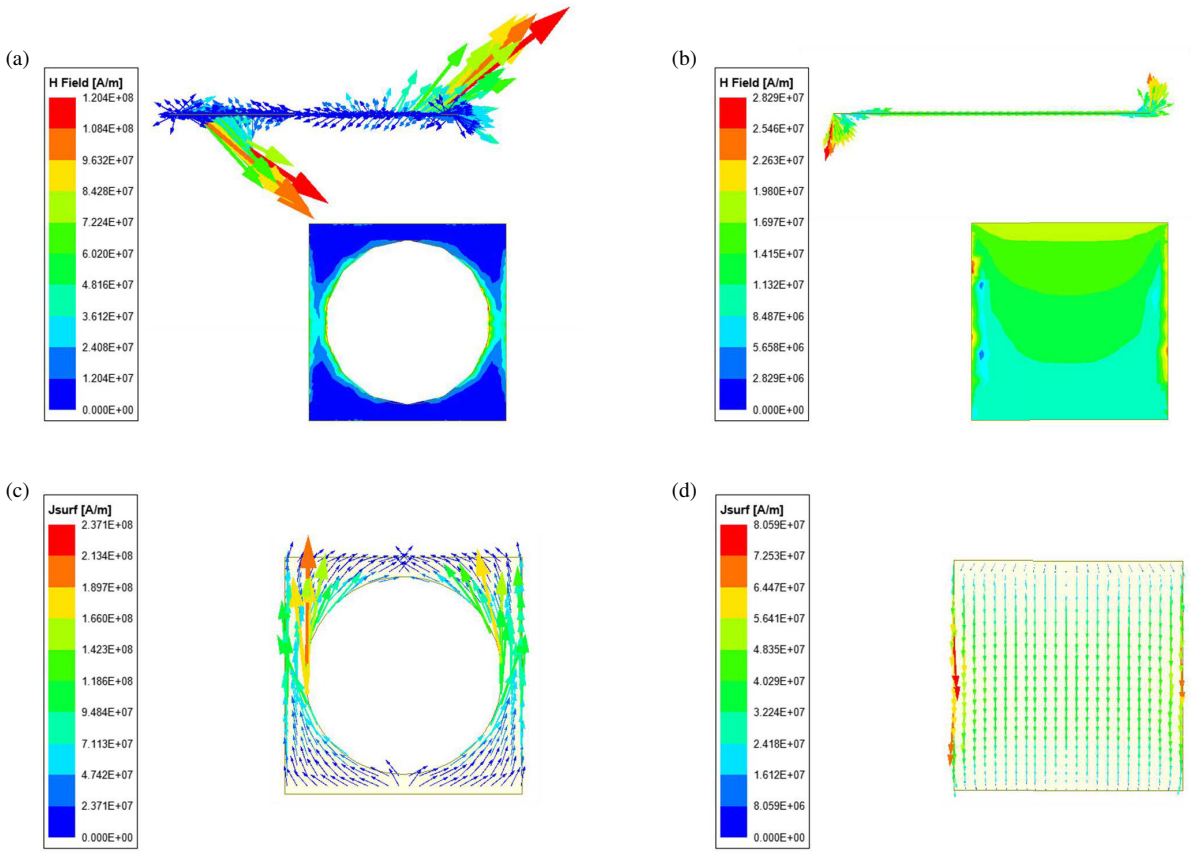

FIGURE 2. (a) Vector field map of magnetic field intensity for OSIC unit. (b) Vector field map of magnetic field intensity for square unit. (c) Vector field map of surface current intensity for OSIC unit. (d) Vector field map of surface current intensity for square unit.

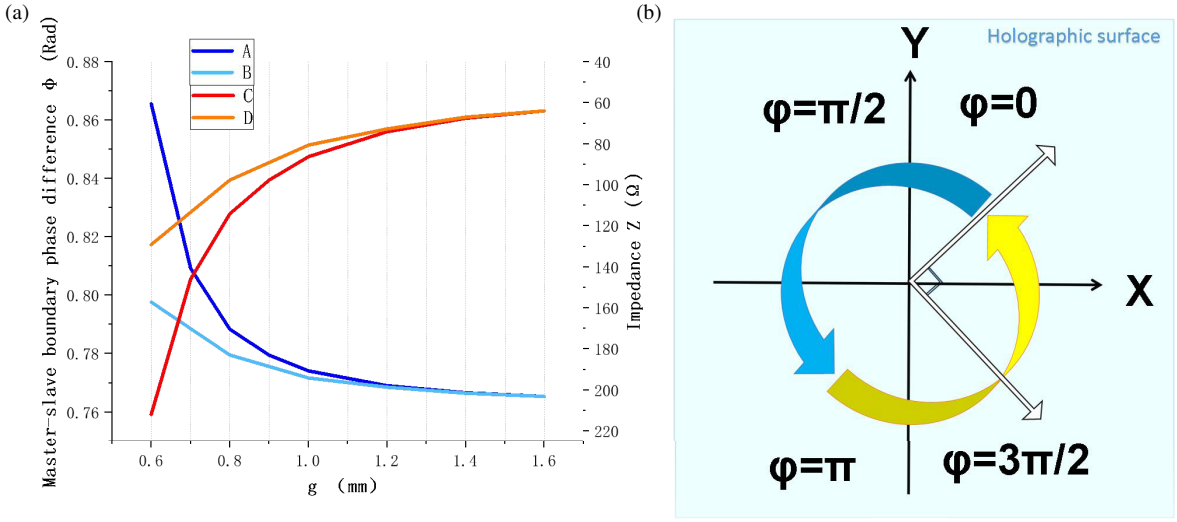

FIGURE 3. (a) A represents the main-slave boundary difference curve for the OSIC unit. B represents the main-slave boundary difference curve for the square unit. C represents the impedance curve for the OSIC unit. D represents the impedance curve for the square unit. (b) Left-handed CP has four loading phase values within the four quadrants of the holographic surface.

slave boundary differences into Equation (2), a one-to-one correspondence between cell spacing and impedance can be obtained. Figure 3(a) illustrates a comparison between the main-slave boundary difference and impedance mapping relationships for the OSIC unit and the square unit. It can be observed that as the unit spacing "g" varies from 0.6 mm to 1.6 mm, the impedance variation range for the OSIC unit is between 212 Ω and 64 Ω, with the main-slave boundary difference change of

0.1002. For the square unit, the impedance variation range is between 129.2 Ω and 64 Ω, with the main-slave boundary difference change of 0.0323. Therefore, it can be calculated that the main-slave boundary difference for the OSIC circle unit compared to the square unit has increased by 210%; the average impedance value "X" has increased by approximately 42.9%; the modulation depth "M" has increased by approximately 127%; and the radiation efficiency "M/X" has increased by approximately 58.9%. As shown by the curve C in Figure 3(a), using the numerical fitting function in MATLAB software yields a functional relationship between cell spacing (g) and impedance (Z):

$$g = 1.237 \cdot 10^{-8} Z^4 - 7.732 \cdot 10^{-6} Z^3 + 1.784 \cdot 10^{-3} Z^2 - 0.182 Z + 7.719 \quad (3)$$

The impedance modulation formula [3] for planar structures is known to be:

$$Z(x,y) = j\left[X + M\mathrm{Re}\left(\psi_{\mathrm{rad}} \times \psi_{\mathrm{ref}}^*\right)\right] \quad (4)$$

where the average impedance (X) is 138 ohms, and the modulation depth (M) is 74 ohms. Ψ_{ref} represents the reference wave expression, and Ψ_{rad} represents the radiation wave expression. When the reference wave illuminates the holographic pattern, the radiation wave can be deduced by computing $\mathrm{Re}(\Psi_{\mathrm{rad}} \times \Psi_{\mathrm{ref}}^*)$.

The feeding expression for the cylindrical waveforms of monopole [22] is:

$$\psi_{\mathrm{ref}} = e^{-jk_t r} = e^{-jk_t\sqrt{x^2+y^2}} \quad (5)$$

where r is the distance from the feed source to any point on the impedance surface along which the surface wave propagates. It should be noted that the monopole needs to have good matching in the operating frequency range, and the phase center needs to match the designed holographic pattern.

The expression for the radiation wave [23] achieving the spatial single-beam angle (θ) is:

$$\psi_{\mathrm{rad}} = e^{-jk_0 x \sin\theta} \quad (6)$$

Equations (5) and (6) are substituted into Equation (4), resulting in:

$$Z(x,y) = j\left[X + M\mathrm{Re}\left(e^{-jk_0 x\sin\theta} e^{jk_t\sqrt{x^2+y^2}}\right)\right] \quad (7)$$

In Figure 3(b), the blue base represents the holographic surface. The loading phase has a period of 2π, with the loading phase in each quadrant increasing left-handedly by $\pi/2$. Any pair of basic sectors separated by a 90° ray will generate orthogonal and quadrature-phased components, thereby achieving CP characteristics [24]. The rotation direction of circularly polarized waves is determined by the impedance surface introducing a 90° phase shift [25]. The modulation formula is represented as:

$$Z(x,y) = j\left[X + M\mathrm{Re}\left(e^{j\varphi} e^{-jk_0 x\sin\theta} e^{jk_t\sqrt{x^2+y^2}}\right)\right] \quad (8)$$

For dual beams [26], each method has its own advantages and disadvantages. Considering the CP effect, the modulation technique used for dual-beam configurations is one that allows for better CP effects but may introduce beam crosstalk. Therefore, the number of beams (K) is set to 2, with angles $\theta_1 = 10°$ and $\theta_2 = 30°$. The impedance modulation formula [19] is as follows:

$$Z(x,y) = j\left[X + \frac{M}{K}\sum_{i=1}^{K}\mathrm{Re}\left(\psi_{\mathrm{rad}_i} \times \psi_{\mathrm{ref}}^*\right)\right] \quad (9)$$

The calculation formula for circularly polarized dual-beam holographic antenna was derived using the four quadrant phase modulation method:

$$Z(x,y) = j\left\{X + \frac{M}{K}\left[\cos\left(\varphi + k_t\sqrt{x^2+y^2} - k_0 x\sin\theta_1\right) + \cos\left(\varphi + k_t\sqrt{x^2+y^2} - k_0 x\sin\theta_2\right)\right]\right\} \quad (10)$$

By substituting the loading phase ψ from Figure 3(b) into Equation (10), we obtain the impedance modulation formula for the antenna design:

$$Z(x,y) = j\begin{cases} X + \frac{M}{K}\left[\cos\left(k_t\sqrt{x^2+y^2} - k_0 x\sin\theta_1\right) + \cos\left(k_t\sqrt{x^2+y^2} - k_0 x\sin\theta_2\right)\right], & x>0; y>0 \\ X - \frac{M}{K}\left[\sin\left(k_t\sqrt{x^2+y^2} - k_0 x\sin\theta_1\right) + \sin\left(k_t\sqrt{x^2+y^2} - k_0 x\sin\theta_2\right)\right], & x<0; y>0 \\ X - \frac{M}{K}\left[\cos\left(k_t\sqrt{x^2+y^2} - k_0 x\sin\theta_1\right) + \cos\left(k_t\sqrt{x^2+y^2} - k_0 x\sin\theta_2\right)\right], & x<0; y<0 \\ X + \frac{M}{K}\left[\sin\left(k_t\sqrt{x^2+y^2} - k_0 x\sin\theta_1\right) + \sin\left(k_t\sqrt{x^2+y^2} - k_0 x\sin\theta_2\right)\right], & x>0; y<0 \end{cases} \quad (11)$$

After corresponding to the specific location and unit spacing, quasi-periodic unit modeling is required. Due to the extensive

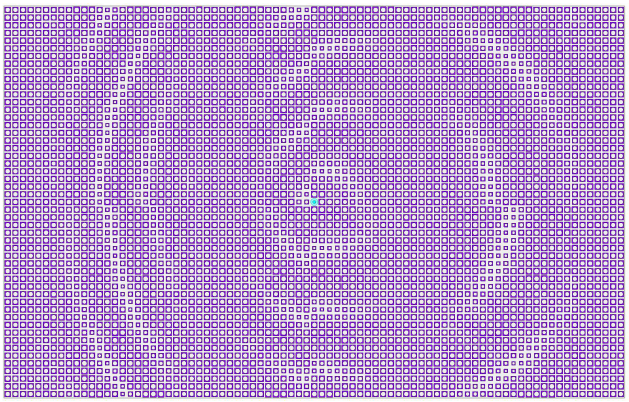

FIGURE 4. Holographic antenna simulation model diagram.

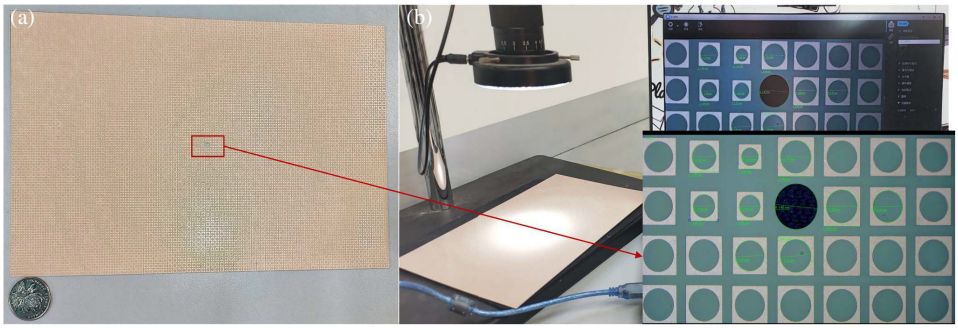

FIGURE 5. (a) Holographic pattern compared to coin size. (b) Left: Microscope measuring antenna unit size environment diagram. Upper right: Real-time electronic size display. Lower right: Enlarged electronic size diagram.

number of units, manual modeling is challenging to achieve. Accordingly, the partition is conducted into four regions based on the distinct phases within the four quadrants. MATLAB is employed to invoke the VBS macro programming feature of electromagnetic simulation software, enabling automated modeling of holographic antennas across the four regions. This approach significantly expedites the overall modeling process.

3. SIMULATION DESIGN AND EXPERIMENTAL MEASUREMENT

The holographic antenna designed in this study is composed of $81 * 51$ OSIC structure elements, with dimensions measuring 243 mm $*$ 153 mm in length and width. The antenna is fed by soldering SMA connectors to the back of the holographic pattern, which has undergone anti-oxidation treatment on its surface. Figure 4 depicts the model of all units of the holographic antenna design. Figure 5(a) compares the size of the holographic pattern with a coin. Figure 5(b) shows the computer equipment connected to a high-definition CCD microscope, displaying and preserving the electronic measurements in real-time. The lower right part is an enlarged image of the electronic dimensions measured by the units within the red circle in Figure 5(a).

Through HFSS simulation, we obtained data such as antenna return loss and dual-beam gain. The antenna was manufactured and tested, with the simulation results compared for validation. As shown in Figure 6, the inset image in the lower left part depicts the environment during the measurement of the antenna using a vector network analyzer. The data obtained is represented by the red line, indicating the measured S_{11}. The blue line represents the S_{11} simulated using HFSS software. The bandwidth below -10 dB ranges from 10.23 GHz to 16.59 GHz. It can be observed that compared to the simulated S_{11} of the holographic antenna, the measured S_{11} shows deviation and a slightly reduced bandwidth, but is nearly identical.

Due to the use of co-modulation techniques to modulate the dual beams, the units will introduce some interference to both beams, resulting in sidelobes in the middle of the dual beams of the antenna. The central angle of one beam may experience slight variations in axial ratio. However, all these effects are within an acceptable range. As shown in Figure 7, the simulation results of the antenna demonstrate its good left-hand circu-

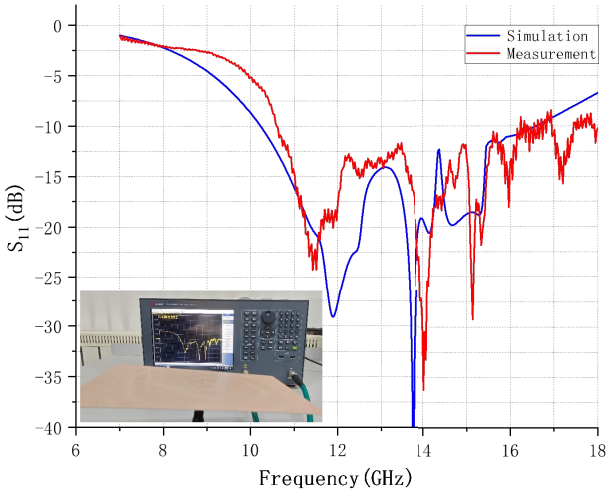

FIGURE 6. Comparison of holographic antenna S_{11} between simulations using HFSS software and measurements using a vector network analyzer.

lar polarization performance. The 3 dB axial ratio beamwidth ranges from 6.08° to 13.4° and from 27.35° to 34.93°, with a total axial ratio beamwidth of 14.9°. In Figure 8, the solid line represents the simulated gain curve of the antenna, with peak gains of 16 dBi and 15.8 dBi, respectively. The image inserted in the upper left part is an environmental image of the antenna gain measured in a microwave anechoic chamber, and its data is displayed with dashed lines. The highest measured gain is 15.61 dBi, indicating a slight reduction in peak gain compared to simulation, and a slight deviation towards lower angles. Compared to the simulated data, the measured data may have errors due to the following reasons: Firstly, the machining accuracy is not precise enough, and the overall antenna is relatively flexible, making it unable to be completely flat, leading to changes in surface impedance. Secondly, the feeding height is not accurately matched, and the feeding position cannot be completely aligned with the phase center during manual soldering, resulting in a deterioration of the match between the feeding and the holographic pattern.

Table 1 compares the parameters with some literature, where (S) is added after the simulated data for additional annotation. The design is compared with both dual-beam and circularly po-

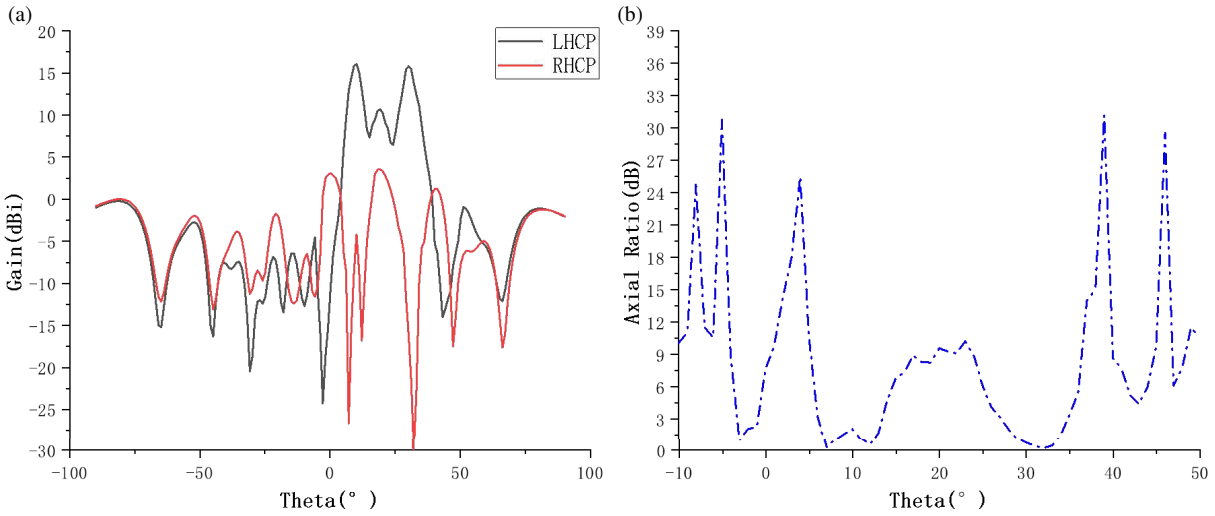

FIGURE 7. Holographic antenna simulation results: (a) Left-hand circular polarization and right-hand circular polarization diagram. (b) Axial ratio diagram.

TABLE 1. Performance comparison between this design and other antennas.

References	Center frequency (GHz)	Holographic profile thickness (mm)	Impedance bandwidth (GHz)	Whether or not CP and the number of beams	Beam angle (°)	Axis ratio beam width (°)	Maximum gain (dBi)
[21]	10	2	9–11	yes; 1	0	6.08	20.8 (S)
[25]	12	1.27	10.2–15.4	yes; 1	30	11.8	17.37 (S)
[10]	15	1.5	13.6–16.8	yes; 1	0	-	21.08
[17]	17	1.575	-	yes; 1	0	7.5	21
[6]	7.2	3	7.2–8^{+}	no; 2	5; 30	-	11.6 (S)
[7]	10	1.52	-	no; 2	0; 10	-	16.1 (S)
[26]	15	1.524	10–16.5	no; 2	32; 42	-	15.9 (S)
[14]	26	1.524	25.2–26.2	no; 3	60; 180; 300	-	14.5 (S)
This design	12	0.635	10.2–16.6	yes; 2	10; 30	14.9	15.61

(S) represents simulated data.

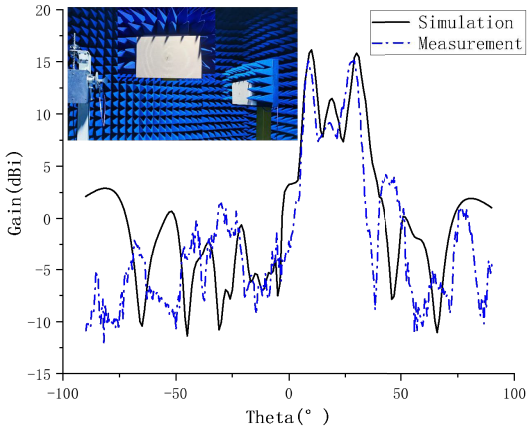

FIGURE 8. Comparison of holographic antenna gain between simulations using HFSS software and measurements conducted in a microwave anechoic chamber.

larized holographic antennas. The comparison results indicate that this design achieves low profile, wide impedance bandwidth, CP beamwidth, and high gain simultaneously.

4. CONCLUSION

In this paper, corresponding formulas were derived using the method of four-quadrant phase modulation. A low-profile holographic dual-beam antenna with CP was proposed. Precise impedance values were extracted from master-slave boundary differences, and OSIC structure elements were utilized to enhance leaky-wave radiation, mitigating the adverse effects of low holographic profiles. Compared to commonly used square units, the master-slave boundary difference has been increased by 210%, and the leaky-wave efficiency has been improved by 58.9%. By employing four different phases for MATLAB partitioned modeling, modeling speed is accelerated, reducing waiting time. Experimental results demonstrate that this design

maintains excellent performance despite its low holographic profile. The impedance bandwidth ranges from 10.23 GHz to 16.59 GHz, with a maximum gain of 16 dBi, and the CP angles for the dual-beam range from 6.08° to 13.4° and from 27.35° to 34.93°. Through simulation, measurement, and experiment comparisons, the feasibility of this holographic antenna design has been demonstrated, providing valuable insights for fields like satellite communication.

REFERENCES

[1] El Sherbiny, M., A. E. Fathy, A. Rosen, G. Ayers, and S. M. Perlow, "Holographic antenna concept, analysis, and parameters," *IEEE Transactions on Antennas and Propagation*, Vol. 52, No. 3, 830–839, Mar. 2004.

[2] Li, M., M.-C. Tang, and S. Xiao, "Design of a LP, RHCP and LHCP polarization-reconfigurable holographic antenna," *IEEE Access*, Vol. 7, 82 776–82 784, 2019.

[3] Fong, B. H., J. S. Colburn, J. J. Ottusch, J. L. Visher, and D. F. Sievenpiper, "Scalar and tensor holographic artificial impedance surfaces," *IEEE Transactions on Antennas and Propagation*, Vol. 58, No. 10, 3212–3221, Oct. 2010.

[4] Zadeh, M. A. C. and N. Komjani, "Flat-topped radiation pattern synthesis of a conformal leaky-wave holographic antenna," *IEEE Transactions on Antennas and Propagation*, Vol. 71, No. 5, 4045–4054, May 2023.

[5] Nannetti, M., F. Caminita, and S. Maci, "Leaky-wave based interpretation of the radiation from holographic surfaces," in *2007 IEEE Antennas and Propagation Society International Symposium*, 5813–5816, IEEE, 2007.

[6] Kampouridou, D. and A. Feresidis, "Tunable multibeam holographic metasurface antenna," *IEEE Antennas and Wireless Propagation Letters*, Vol. 21, No. 11, 2264–2267, Nov. 2022.

[7] Nguyen, T. D., T. H. Y. Nguyen, and G. Byun, "Multi-beam holographic metasurface antenna using stepped-impedance distributions," in *2023 IEEE International Symposium on Antennas and Propagation (ISAP)*, 1–2, Kuala Lumpur, Malaysia, 2023.

[8] Rusch, C., S. Beer, P. Pahl, and T. Zwick, "Multilayer holographic antenna with beam scanning in two dimensions at W-band," in *2013 7th European Conference on Antennas and Propagation (EuCAP)*, 2625–2628, Gothenburg, Sweden, 2013.

[9] Zhu, L., Y. Liu, and Y. Jia, "A high-gain circularly-polarized holographic antenna based on impedance-modulated surface," in *2020 Cross Strait Radio Science & Wireless Technology Conference (CSRSWTC)*, 1–3, Fuzhou, China, 2020.

[10] Wang, J. and R. Yang, "Generating high-purity directive circularly polarized beams from conformal anisotropic holographic metasurfaces," *IEEE Transactions on Antennas and Propagation*, Vol. 70, No. 11, 10 718–10 723, Nov. 2022.

[11] Su, T., Q. Zhang, R. Chen, and C. Sun, "Novel design of surface-wave holographic antenna miniaturization," *IEEE Antennas and Wireless Propagation Letters*, Vol. 14, 1077–1080, 2015.

[12] Liu, Y., N. Li, Y. Jia, W. Zhang, and Z. Zhou, "Low RCS and high-gain patch antenna based on a holographic metasurface," *IEEE Antennas and Wireless Propagation Letters*, Vol. 18, No. 3, 492–496, Mar. 2019.

[13] Kong, X., Y. Tian, Q. Feng, and L. Li, "High-efficiency cylindrical conformal holographic metasurface based on tensor impedance modulation surface," in *2022 IEEE MTT-S International Wireless Symposium (IWS)*, Vol. 1, 1–3, Harbin, China, 2022.

[14] Zadeh, M. A. C., N. Komjani, and S. Zohrevand, "Multibeam 5G conical leaky-wave antenna based on holographic technique," in *2022 6th International Conference on Millimeter-Wave and Terahertz Technologies (MMWaTT)*, 1–5, Tehran, Iran, Islamic, 2022.

[15] Xue, S., Y. Shen, and S. Hu, "Dual circularly-polarized holographic metasurface antenna," in *2020 13th UK-Europe-China Workshop on Millimetre-Waves and Terahertz Technologies (UCMMT)*, 1–3, Tianjin, China, 2020.

[16] Liu, Y., L. Zhu, and Y. Jia, "A wideband low-radar cross section circularly polarized holographic antenna based on hybrid metasurface," *International Journal of RF and Microwave Computer-Aided Engineering*, Vol. 32, No. 1, e22917, 2022.

[17] Kim, S., D. Shrekenhamer, J. Will, R. Awadallah, and J. Miragliotta, "High impedance holographic metasurfaces for conformal and high gain antenna applications," in *2018 15th IEEE Annual Consumer Communications & Networking Conference (CCNC)*, 1–4, Las Vegas, NV, USA, 2018.

[18] Lv, H.-H., Q.-L. Huang, J.-L. Liu, J.-Q. Hou, and X.-W. Shi, "Holographic design of beam-switchable leaky-wave antenna," *IEEE Antennas and Wireless Propagation Letters*, Vol. 18, No. 12, 2736–2740, Dec. 2019.

[19] Movahhedi, M., M. Karimipour, and N. Komjani, "Multibeam bidirectional wideband/wide-scanning-angle holographic leaky-wave antenna," *IEEE Antennas and Wireless Propagation Letters*, Vol. 18, No. 7, 1507–1511, 2019.

[20] Li, J., C. Yang, Q. Chen, B. Li, and X. He, "Millimeter-wave circularly polarized holographic antenna based on artificial impedance surface," *Journal of Terahertz Science and Electronic Information Technology*, Vol. 14, No. 4, 581–585, 2016.

[21] Gan, L., W. Jiang, S. Gong, Q. Chen, and X. Li, "A low-profile and high-gain circularly polarized antenna based on holographic principle," in *2018 Asia-Pacific Microwave Conference (APMC)*, 1031–1033, Kyoto, Japan, 2018.

[22] Wang, Y.-D., D. Wang, J. Zhao, L.-Z. Yin, Y.-H. Tan, and P.-K. Liu, "Active holographic metasurface for electrically controllable 2-D beam scanning," in *2021 International Conference on Microwave and Millimeter Wave Technology (ICMMT)*, 1–3, Nanjing, China, 2021.

[23] Jia, Y., Y. Liu, Y. Feng, and Z. Zhou, "Low-RCS holographic antenna with enhanced gain based on frequency-selective absorber," *IEEE Transactions on Antennas and Propagation*, Vol. 68, No. 9, 6516–6526, Sep. 2020.

[24] Minatti, G., F. Caminita, M. Casaletti, and S. Maci, "Spiral leaky-wave antennas based on modulated surface impedance," *IEEE Transactions on Antennas and Propagation*, Vol. 59, No. 12, 4436–4444, Dec. 2011.

[25] Zhang, J., "Scropue holographic impedance surface antenna design," Ph.D. dissertation, Xi'an University of Electronic Science and Technology, Xi'an, China, 2019.

[26] Eltersy, N. A., H. A. Malhat, and S. H. Zainud-Deen, "Dual-beam conformal hologram metasurface leaky wave antenna based on surface impedance modulation," in *2023 40th National Radio Science Conference (NRSC)*, Vol. 1, 9–16, Giza, Egypt, 2023.